

Influence of Vibration in the Nozzle Frame on the Ribbon Characterization in Planar Flow Melt Spinning Process



Meenuga ShanthiRaju , Anil Kumar Birru , and Sowjanya Madireddi 

1 Introduction

The PFMS process is a continuous casting approach for manufacturing thinner, wider, and continuous amorphous/nanocrystalline metal ribbons by rapid solidification technique [1–3]. This process has been enormously gain interest in industry and academic research because of the environmental and economic advantages of final casting product [4–6]. On the one hand, Fe-based amorphous ribbons have deficiency of long-range structural imperfection, exhibit large elastic strain restriction, excellence in strength, good wear, and corrosion resistance [7–10]. On the other hand, nanocrystalline ribbons have exclusive combination of enlarged physical, chemical, thermal, and mechanical properties [8, 9]. The effect of predominant process parameters such as quenching wheel speed (U), nozzle wheel gap (G), melt ejection pressure (P), and melting temperature (T) was studied on ribbon surface topography [10–12]. The foremost factors for formation of ribbon structure which are including characteristics of nucleation, kinetic crystal growth, internal readjustment of heat, and external heat extraction [13].

The defected casting lines appeared on the surface of the ribbon due to meniscus holding subjected to melt motion. Also, they mentioned cross lines were similar to the herringbone line but difference wavelength [14]. The dimples and striation lines are avoided within the specified range of Stefan number in the 50Pb-50Sn alloy. This criterion was not successful for all alloy systems. A continuous cross wave or herringbone defect lines were studied by correlating between the meniscus frequency and wave lines [15]. Theisen, Huang et al. [16, 17] observed that the

M. ShanthiRaju (✉) · A. K. Birru
National Institute of Technology, Manipur 795004, India
e-mail: shantimr@gmail.com

S. Madireddi
CVR College of Engineering, Hyderabad, Telangana 501510, India

herringbone defect occurred at lower over pressure than the cross wave line defects. In addition, they have scaled herringbone and cross wave lines with capillary frequency $(\sigma/\rho g^3)^{1/2}$, where σ is surface tension, g is the nozzle wheel gap, and ρ is density of liquid. Despite of above work, the mechanism of herringbone defect formation largely remained unclear.

Nevertheless, amorphous alloys can also failure by cavitation instabilities [10, 18, 19]. The shear bands affected to be nucleated in amorphous materials failure in microscopic level under dynamic and quasistatic loads [9, 19, 20]. The mechanism of cavitation inception in brittle materials is due to fluctuation of atomic density initiate at weak zones to reduce the yield strength [21]. The prognosis of void growth in cavitation instability explained through single spherical void model and the theory of free volume [10]. Further investigation has been carried out by [20] cavitation instability is remarkable decreased by the weak zones and it does not decreased at stress ratio reduced from unity. Also, they observed the spallation causes fracture in amorphous materials like micro dimple nucleation, porous, and equiaxed cellular growth on the surface of the ribbon. The formation of defects on solidified surface of the ribbon was due to dynamic variation in pressure distribution, density of melt, solidification temperature, and motion of the quenching wheel [22]. Moreover, the concentration has been taken to examination of cavitation instability on regular crystalline materials rather on amorphous alloys. In this present research, we focused on the influence of vibration at the liquid ejected nozzle frame, which is directly affected on the melt puddle morphology and solidified ribbon surface.

2 Experimental

The titular composition $\text{Fe}_{73.5}\text{Si}_{13.5}\text{B}_9\text{Nb}_3\text{Cu}_1$ of basic alloy has prepared in induction melting furnace at 1×10^{-5} mbar of vacuum level under complete control of argon gas. The alloy was prepared for 100 g weight percentage by using economically available materials. The alloy composition of Fe-B (15.37 wt. %), Fe-Si (12.69 wt. %), and (Fe-Nb 7.73 wt. %), pure Fe 62.94 wt. % and pure Cu 1.30 wt. % and additionally for evaporation loses an extra 10% Boron has added [22]. The chemical homogeneity test has been conducted to ensure the homogeneity of basic alloy. The atomic weight percentages of this fundamental nominal alloy are compare with the analyzed alloy. The results of nominal and analyzed atomic weight percentages are given in Table 1.

Table 1 The atomic weight percentages of analyzed and nominal alloy compositions [22]

Composition	Fe (at%)	B (at%)	Si (at%)	Nb (at%)	Cu (at%)
Analysis	72.84	9.52	13.6	3.03	1
Nominal	73.5	9	13.5	3	1

Table 2 The process parameters for experimentation

Exp. No.	Weight of alloy (g)	Wheel speed (U) (m/s)	Ejection pressure (P) (kpa)	Nozzle wheel gap (G) (mm)	Melt temperature (T) (K)
1	122	30	7	0.35	1575
2	104	30	14	0.35	1575
3	101	30	21	0.35	1575

The liquid is ejected nearly at critical temperature ($T_c = 1350^\circ\text{C}$) from the quartz crucible nozzle slit gap 0.3 mm. The quenching wheel speed $U = 30\text{ m/s}$, nozzle wheel gap $G = 0.35\text{ mm}$, and the melt temperature $T = 1575\text{ K}$ have taken constant throughout the experimentation, and ejection pressure varied as 7, 14, and 21 kPa. The process parameters for experimentation are given in Table 2.

The puddle formation was captured using the images obtained from the high speed videography at a rate 100 frames/sec (Falcon 1.4M100, Dalsa waterloo, Ontario, Canada). The length of the puddle which touched the wheel surface was measured by Imagepro plus software.

3 Results and Discussion

The predominant process parameters for Fig. 1 are $T = 1575\text{ K}$, $U = 30\text{ m/s}$, $G = 0.35\text{ mm}$, $P = 7\text{ kPa}$, and alloy weight is 122 g. The characteristics of the solidified ribbon for experiment 1 are given in Table 3.

Figure 1 shows the high speed images of puddle evolution in between nozzle wheel gap. The experiment starts from liquid ejection at 0 ms and ends at 600 ms. Figure 2a explains the stable length of the puddle on the rotating chilled copper wheel surface with time. A continues ribbon is obtained at firmness of the puddle from 51 to 520 ms and the puddle length varies from 0.823 to 0.876 mm. Figure 2b gives the nozzle wheel gap (G) which also equal to height of the puddle is varied from 0.3768 to 0.3869 mm during the steadiness of the puddle. The actual maintained gap $G = 0.35\text{ mm}$ is varied due to vibration in the ejection nozzle slit. A continues ejection of liquid on the rotating chilled wheel surface from the nozzle slit gap ($g = 0.3\text{ mm}$) causes the upthrust or buoyancy force and the surface tension of the liquid slightly lift the nozzle frame. Due to this vibrational effect, the fluctuation generates in puddle morphology. According to the fluid mechanism concepts the compressive stress in the puddle fluid medium between the rotating chilled substrate and nozzle bottom surface. When the fluid is subjected to rapid compression stress due to ejection pressure on the rotating chilled substrate, the internal resistance force of the fluid particles may increases during solidification at boundary layer. The solidified particles try to push up the nozzle frame slightly, and the fluid may undergo shear stress by the drag force of the quenching wheel. The upward resistance force of the fluid and shear stress due

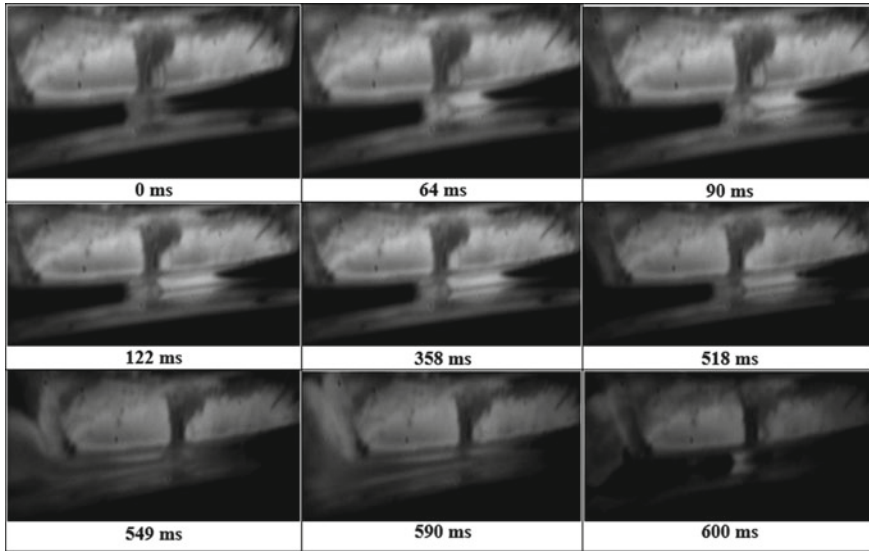


Fig. 1 High speed images of puddle evolution in between nozzle wheel gap for experiment 1

Table 3 The solidified ribbon morphology for experiment 1

Exp. No.	Structure	Length (m)	Average width (mm)	Average thickness (μm)	Surface roughness (μm)
1	Amorphous	9	17	37.3	1.21

to wheel drag causes a small vibration in the nozzle frame. When the fluctuation or vibration of the nozzle frame is at upper position, the pressure may drop at bottom and upper edges of the upstream meniscus (USM). The drag force of the quenching wheel speed entraps surrounded air into liquid puddle from the edges of downstream meniscus (DSM). The regular fluctuations in the puddle and entrapment of air act as thermal resistance at the boundary layer of the wheel substrate may exhibits the herringbone defect on the surface of the ribbon. Figure 3 shows a regular herringbone defect pattern on solidified ribbon surface, and its contour plot color mapping shows the single wavelength.

The two fundamental mechanisms have given [23] for any aspect with an attribute stream wise wave length on continuous casting product. In the first, the template transfer formation mechanism is simply doubling the wheel speed is not affected wave length. In the second, pulse transfer formation mechanism is simply doubling the wheel speed will double the wavelength of the aspect since, the wheel rotate twice then the impingement action. Moreover, the dependence or not of the wavelength but the wheel speed is key to determine the cross wave formation in physics.

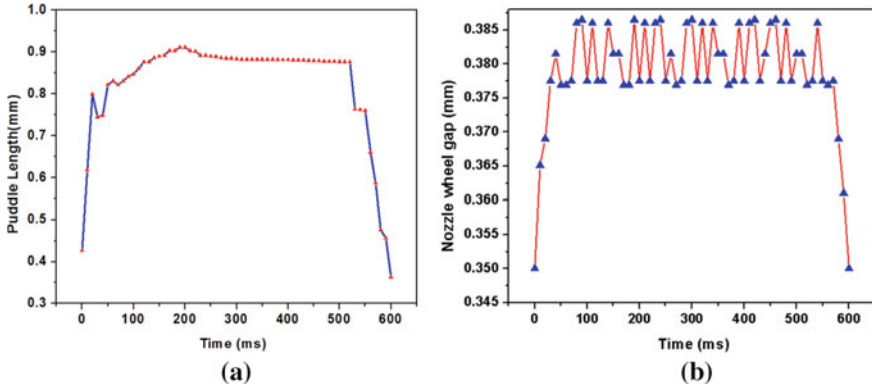


Fig. 2 a Length of the puddle verses to time, b nozzle wheel gap verses to time for experiment 1

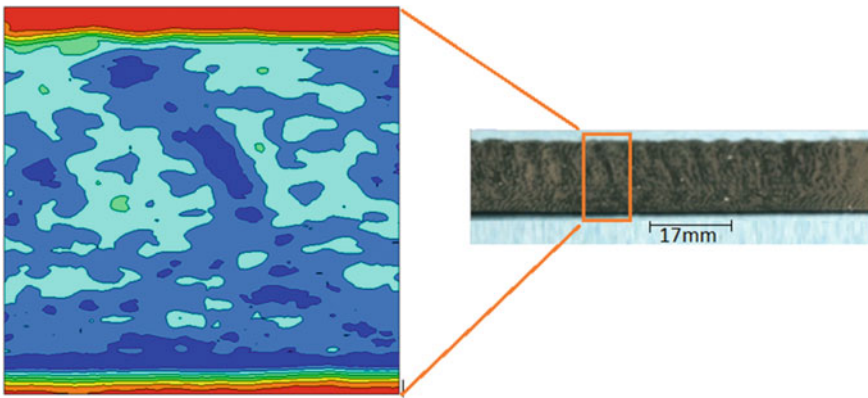


Fig. 3 Regular herringbone defect pattern on solidified ribbon surface and its contour plot color mapping shows the single wavelength

The process parameters for Fig. 4 are $T = 1575 \text{ K}$, $U = 30 \text{ m/s}$, $G = 0.35 \text{ mm}$, $P = 14 \text{ kPa}$, and alloy weight is 104 g. The characteristics of the ribbon for experiment 2 are given in Table 4.

Figure 4 shows the high speed images of puddle development in between nozzle quenching wheel gap for experiment 2. From Fig. 5a and b experiment starts from liquid ejection pressure at 0 to 461 ms. A continues ribbon obtained at firmness of the puddle from 163 to 407 ms and the puddle length varies from 0.883 to 1.05 mm. The nozzle wheel gap (G) or height of the puddle is varied from 0.385 to 0.3961 mm during the steadiness of the puddle.

The length and height of the puddle increased as increasing the ejection pressure from 7 to 14 kPa. The ribbon morphology is greatly affected by the ejection pressure and puddle geometry. By increasing the ejection pressure, both the length and height of the puddle increased. When the nozzle wheel gap or height of the puddle is high,

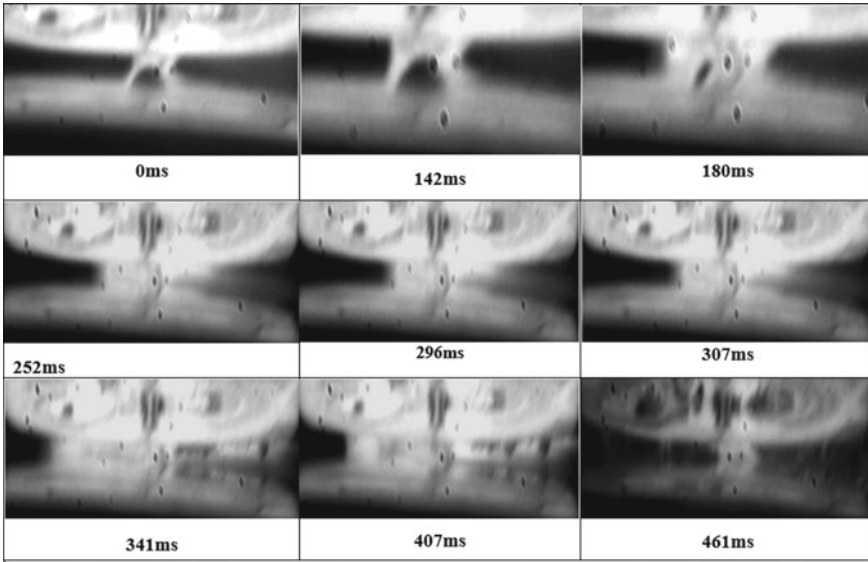


Fig. 4 High speed images of puddle evolution in between nozzle wheel gap for experiment 2

Table 4 Gives the ribbon morphology for experiment 2

Exp. No	Structure	Length (m)	Average width (mm)	Average thickness (μm)	Surface roughness (μm)
2	Amorphous and partial crystalline	12	18	60.6	1.24

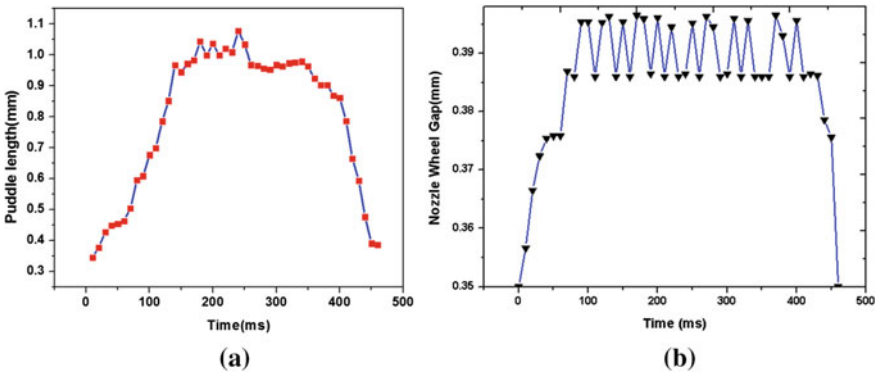


Fig. 5 **a** the length of the puddle verses to time, **b** nozzle wheel gap verses to time for experiment 2

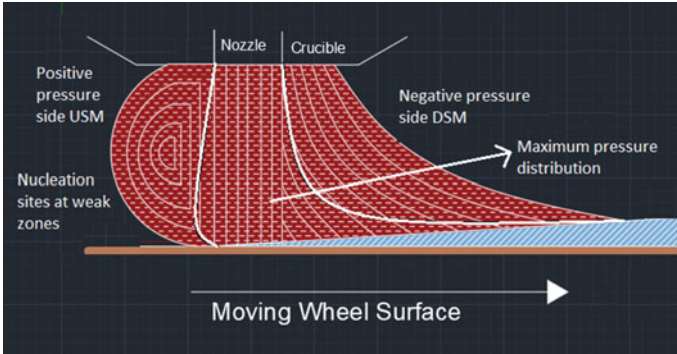


Fig. 6 Pressure distribution at nucleation sites weak zones USM and DSM and formation puddle

the entrapment of air is more from the USM. The simulation work [24] gives the maximum distribution of pressure in the puddle is about five times at lower ejection pressure, and not even doubled in case of higher ejection pressure. Consequently, a radical reduction of pressure at both sides DSM and USM with same magnitude of negative and positive sign. The maximum distribution of increased pressure irrespective of the ejection pressure is resolved only at mid portion of the puddle. The representation of the puddle formation in between the nozzle and on the quenching wheel surface in Fig. 6.

According to assumptions of classical thermodynamic theory predict the initiation of nucleation and kinetic crystal growth starts at weak zones where relatively low pressure, i.e., the bottom edge of USM. It is interesting to notify the formation of porosity at nearly micron level on surface of ribbon. This may be the cause of cavitation effect due to accelerated changes in pressure in the liquid puddle zone. Since the ejection of liquid is about to the critical temperature $T_c = 1350\text{ }^\circ\text{C}$, where the formation of vapor bubbles in liquid phase of the puddle [25]. The vapor bubbles get solidified near at the boundary layer of chilled wheel substrate and formed as

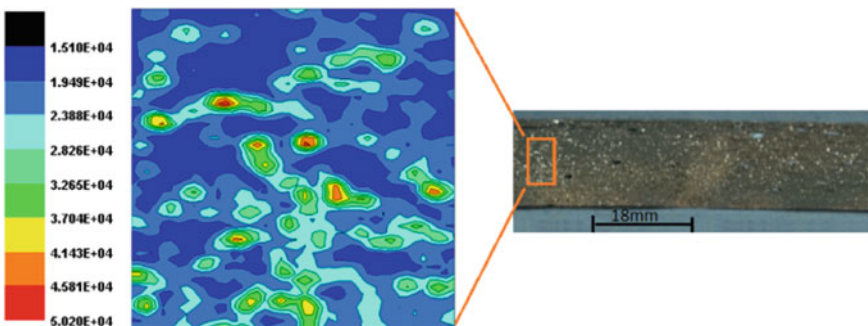


Fig. 7 Tiny porous formations on ribbon surface and contour plot color mapping

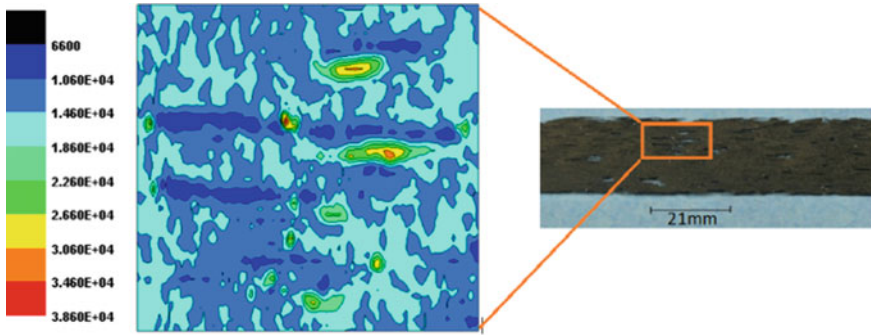


Fig. 8 Grooves and patches on ribbon formation and contour plot color mapping of the surface of the ribbon

Table 5 The ribbon morphology for experiment 3

Exp. No	Structure	Length (m)	Average width (mm)	Average thickness (μm)	Surface roughness (μm)
3	Crystal	6	21	85.3	1.52

tiny porous on the ribbon surface. Figure 7 shows the porous formation on ribbon surface.

The process parameters for Fig. 8 are $T = 1575 \text{ K}$, $U = 30 \text{ m/s}$, $G = 0.35 \text{ mm}$, $P = 21 \text{ kPa}$, and alloy weight is 101 g, and ribbon characteristics are shown in Table 3. The defect forms of small patches are appeared on the surface of the ribbon due to irregular profiled in the formation of puddle. The current results have confirmed to [26–28] at higher ejection pressure the thickness of the ribbon increased. At higher ejection pressure, the possibility of increment in viscosity of liquid flow on the moving wheel substrate may not be properly lingered. The formation of USM and DSM is broken due to surface tension of puddle and air interfaces which results the greater allure between the cohesion of fluid molecule and adhesion of air molecules. The imbalanced force between the fluid and air molecules the fluid become under tension. This behaves like elastic membranes so that the irregular contact of the puddle onto the quenching wheel during solidification process. Under these conditions, the formation of grooves and patches on the surface of the ribbon. The solidified ribbon has become fully crystalline and broken in nature. Table 5 gives the results of the third experiment.

4 Conclusion

1. The fluid is subjected to rapid compression stress due to ejection pressure on the rotating chilled substrate. The internal resistance (buoyancy) force of the fluid

- particles, surface tension, and shear stress due to wheel drag results vibration the nozzle frame. The regular fluctuation in the puddle and entrapment of surrounded air acts like thermal resistance at melt wheel contact may exhibits the herringbone defect on the ribbon surface.
2. The initiation of nucleation and kinetic crystal growth begins at the USM, where pressure is relatively low. The variation of pressure in the puddle accelerates may cause to formation tiny vapor bubbles due to cavitation inception. These vapor bubbles in the puddle get solidified at the boundary layer of the wheel substrate results porosity on the ribbon surface.
 3. At higher ejection pressure, the formation USM and DSM broke due to imbalanced force between the entrapped air and fluid molecules so that the puddle behaves like elastic membranes under tension. The irregular contact between the puddle and wheel substrate results patches and grooves on the ribbon surface.

Acknowledgements Authors would like to thankful to Defence Metallurgical Research Laboratory, Hyderabad, to carry out the current collaboration research work with NIT Manipur. Author 1 sincerely grateful Dr. Bhaskar Majumdar Sc. 'F' for all his technical backing and sparing time.

References

1. Narasimhan M (1979) Continuous casting method for metallic strips. U.S. Patent No. 4,142,571
2. Steen PH, Karcher C (1997) *Annu Rev Fluid Mech* 29:373–97
3. Altieri AL, Steen PH (2014) *J Thermal Sci Eng Appl* 6:1-9
4. Hasegawa R (2000) Present status of amorphous soft magnetic alloys. *J Magn Magn Mater* 215:240–245
5. Kumar K, Van Swygenhoven H, Suresh S (2003) Mechanical behavior of nanocrystalline metals and alloys. *Acta Mater* 51:5743–5774
6. Gleiter H (1989) Nanocrystalline materials. In: *Progress in materials science*, vol 33, Elsevier pp 223–315
7. Trudeau M, Ying J (1996) Nanocrystalline materials in catalysis and electrocatalysis: structure tailoring and surface reactivity. *Nanostruct Mater* 7:245–258
8. Suryanarayana C, Koch C (2000) Nanocrystalline materials—current research and future directions. *Hyperfine Interact* 130:5
9. Huang X, Ling Z, Zhang HS, Ma J, Dai LH (2011) How does spallation micro damage nucleate in bulk amorphous alloys under shock loading? *J Appl Phys* 110
10. Jiang MQ, Wang WH, Dai LH (2009) Prediction of shear-band thickness in metallic glasses. *Scripta Mater* 60:1004–1007
11. Majumdar B, Sowjanya M, Srinivas M, Babu DA, Kishen T, Reddy K (2012) *Trans Indian Inst Met* 65(6):841–847.
12. Clyne TW (1984) Numerical treatment of rapid solidification. *Metall Trans B* 15B:369–381
13. Carpenter J, Steen P (1992) Planar-flow spin-casting of molten metals: process behaviour. *J Mater Sci* 27(1):215–225
14. Byrne C, Theisen E, Reed B, Steen P (2006) Capillary puddle vibrations linked to casting-defect formation in planar-flow melt spinning. *Metall Mater Trans B* 37B:445–456
15. Praisner T, Chen J, Tseng A (1995) An experimental study of process behavior in planar flow melt spinning. *Metall Mater Trans B* 26(1):1199–1208

16. Theisen E (2007) Transient behavior of the planar-flow melt spinning process with capillary dynamics. Cornell University (Ph.D. thesis)
17. Huang X, Ling Z, Wang YJ, Dai LH (2016) Intrinsic structural defects on medium range in metallic glasses. *Intermetallics* 75:36–41
18. Huang X, Ling Z, Dai LH (2019) Influence of surface energy and thermal effects on cavitation instabilities in metallic glasses. *Mech Mater* 131:113–120
19. Huang X, Ling Z, Dai LH (2013) Cavitation instabilities in bulk metallic glasses. *Int J Solids Struct* 50:1364–1372
20. Singh I, Guo TF, Murali P, Narasimhan R, Zhang YW, Gao HJ (2013) Cavitation in materials with distributed weak zones: implications on the origin of brittle fracture in metallic glasses. *J Mech Phys Solids* 61:1047–1064
21. Murali P, Guo TF, Zhang YW, Narasimhan R, Li Y, Gao HJ (2011) Atomic scale fluctuations govern brittle fracture and cavitation behavior in metallic glasses. *American Phys Soc, PRL*. 215501 vol 107, pp 1–5
22. Meenuga S, Kumar BA, Kumar BP (2021) Effect of cavitation and spallation on ribbon morphology of Fe_{73.5}Si_{13.5}B₉Cu₁Nb₃ alloy in planar flow melt spinning process. *Mater Today: Proc* <https://doi.org/10.1016/j.matpr.2021.05.121>
23. Byrne CJ, Theisen EA, Reed BL, Steen PH (2006) *Metall Mater Trans B Process Metall Mater Process Sci* 37:445–456
24. Sowjanya M, Reddy TKK (2014) *J Mater Process Technol* 214:1861–1870
25. Gao H, Li Z, Zhou S, Zhang G, Cui N (2019) *Prog Nat Sci Mater Int* 29:556–560
26. Tkatch VI, Limanovskii AI, Denisenko SN, Rassolov SG (2002) The effect of the melt-spinning processing parameters on the rate of cooling. *Mater Sci Eng, A* 323(1–2):91–96
27. Srinivas M, Majumdar B, Phanikumar G, Akhtar D (2011) Effect of planar flow melt spinning parameters on ribbon formation in soft magnetic Fe_{68.5}Si_{18.5}B₉Nb₃Cu₁ alloy. *Metall Mater Trans B*, 42(2), 370–379
28. Bouchbinder E, Langer JS, Procaccia I (2007) *Phys Rev E—Stat Nonlinear Soft Matter Phys* 75:1–9